JOURNAL OF APPLIED PHYSICS **104**, 123533 (2008)

Strain evolution in Al conductor lines during electromigration

H. Zhang,[1,a)] G. S. Cargill III,[1] Y. Ge,[2] A. M. Maniatty,[2] and W. Liu[3]
[1]*Department of Materials Science and Engineering, Lehigh University, Bethlehem, Pennsylvania 18105, USA*
[2]*Department of Mechanical, Aerospace & Nuclear Engineering, Rensselaer Polytechnic Institute, Troy, New York 12180, USA*
[3]*Advanced Photon Source, Argonne National Laboratory, Argonne, Illinois 60439, USA*

(Received 6 August 2008; accepted 28 October 2008; published online 31 December 2008)

Monochromatic and white beam synchrotron x rays were used to study the deviatoric strains and full elastic strains in passivated Al conductor lines with near-bamboo structures during electromigration (EM) at 190 °C. A strong strain gradient formed in the upstream part of the Al lines. Strains along the downstream part of the lines were smaller and more scattered. Numerical analysis using the Eshelby model and finite element method (FEM) calculations suggest that the moving of atoms during EM in these near-bamboo Al lines is dominated by top and/or bottom interface diffusion, which differs from the reported results for nonbamboo, polycrystalline Al conductor lines, where EM is mainly along the grain boundaries. Local strain measurements and FEM calculations indicate that the EM flux is also nonuniform across the width of the conductor line because of stronger mechanical constraint by the passivation layer near the edges of the line. Plastic deformation is observed during EM by changes in the Laue diffraction patterns. The effective valence $|Z^*| = 1.8 \pm 0.4$ is determined from the measured strain gradient. © *2008 American Institute of Physics*. [DOI: 10.1063/1.3041152]

I. INTRODUCTION

Electromigration (EM) is the movement of atoms caused by flowing electrical current, in which the electrons transfer momentum to atoms.[1] The divergence of mass transport or flux in a metal line can create voids or extrusions that can result in changes in resistance and lead to open or short circuits.[2] EM is one of the major causes of failures of interconnects in integrated circuits. With the scaling down of the dimensions of electronic devices, current densities are increased, and EM becomes more important as a failure mechanism.[3,4]

It is generally assumed that the atom flux J during EM can be expressed as[5]

$$J = -n\frac{D_{\mathrm{eff}}}{kT}\left[|Z^*|ej\rho - b\frac{\partial\sigma_{\mathrm{EM}}}{\partial y}\Omega\right], \tag{1}$$

where n is the atomic density, D_{eff} is the effective diffusion coefficient, k is the Boltzmann constant, T is the absolute temperature, Z^* is the effective valence of the diffusing species, e is the electron charge, j is the current density, ρ is the electrical resistivity of the conductor line, Ω is the atomic volume, $\partial\sigma_{\mathrm{EM}}/\partial y$ is EM-induced stress gradient along the length of the conductor line, and b is a stress state-dependent coefficient, with $b=2/3$ if σ_{EM} is assumed to be an equibiaxial stress and $b=1$ if σ_{EM} is the hydrostatic stress (tensile stress taken as positive).[6] For a conductor line with flux blocking boundaries at both ends and embedded in dielectric material, there exists a critical current density j_c,[5] and for currents below j_c, the stress gradient developed eventually counterbalances the electron wind force, the net atom flux becomes zero, and a linear stress gradient extends over the full length of the conductor line. The effective valence Z^* can be determined from the steady-state stress gradient $(\partial\sigma_{\mathrm{EM}}/\partial y)$ measured for a current density j below j_c.

Synchrotron x-ray microdiffraction can provide measurements of strains in crystalline materials with micron and submicron scale spatial resolution. Wang *et al.*[6] studied EM-induced strain distributions in 200 μm long, 10 μm wide aluminum conductor lines in 1.5 μm SiO_2 passivation layers in real time using synchrotron white beam x-ray microdiffraction with a 10 μm spatial resolution. Their results showed that a steady-state linear stress gradient along the length of the line developed during EM and that the stress gradient could be manipulated by controlling the magnitude and the direction of the current flow.

Theoretical and computational models for predicting stresses/strains that build up during EM, combined with experimental measurements of local strains, can provide insight into the underlying diffusional mechanisms and the effects of line geometry and confining materials. Korhonen *et al.*[7] derived an analytic model of EM, which they applied to a columnar aluminum metallization. In that work, the stress resulting from atoms being deposited in columnar grain boundaries is modeled using the Eshelby theory of inclusions,[8] which treats the interconnect line as an elliptic cylinder embedded in an infinite silicon matrix. Hau-Riege and Thompson[9] performed three-dimensional finite element (FE) analyses considering the effect of surrounding confinement material and the line aspect ratio on the effective modulus, which is related to the rate of stress buildup and EM-induced damage. They considered three possible diffusion paths: (i) diffusion through the grain boundaries for a three-dimensional grain structure, (ii) diffusion through the grain

a)Electronic mail: hoz204@lehigh.edu.

 © 2008 American Institute of Physics

Downloaded 16 Feb 2011 to 128.113.218.36. Redistribution subject to AIP license or copyright; see http://jap.aip.org/about/rights_and_permissions

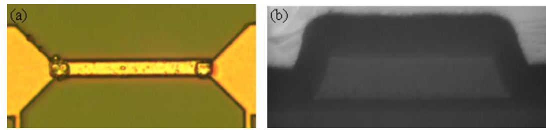
FIG. 1. (Color online) (a) Optical image of the Al line. (b) SEM image after FIB sectioning shows the cross section of the Al line. Sample was tilted 60°.

boundaries for a columnar grain structure, and (iii) surface diffusion, along the top and bottom surfaces of the line. They compared their FE results to those obtained using the Eshelby model presented by Korhonen *et al.*,[7] and they found that the Eshelby model, for the cases considered, did not give accurate predictions.

In this paper, we report grain-scale strain and crystal orientation measurements by x-ray microdiffraction. We discuss the experimental results and compare them to numerical results obtained with an Eshelby model and FE calculations, assuming different possible EM diffusion paths. We also study plastic deformation and microstructure evolution of the Al line during EM. Preliminary reports of this work were given in Refs. 10 and 11.

II. DESCRIPTION OF SAMPLES AND EXPERIMENT

The samples studied are 30 μm long, 2.6 μm wide, and 0.75 μm thick Al conductor lines, with Ti vias and Ti rich top and bottom layers. Figure 1(a) shows an optical image of the Al conductor line and Fig. 1(b) shows a scanning electron microscope (SEM) image of the cross section after focused ion beam (FIB) sectioning. The interlayer dielectric material is SiO_2 and the passivation layer is also SiO_2, 0.7 μm thick. Schematic cross sections and dimensions of the Al line are shown in Figs. 2(a) and 2(b) before reaction of the Ti and Al layers. The TEM image in Fig. 3 shows that the conductor line consists of micron-size columnar grains of about ~0.35 μm thickness. On the top and bottom surfaces of the large grain Al line are smaller (<100 nm) grain size polycrystalline layers, each about 0.2 μm thick, probably mixtures of Al and $TiAl_3$.

X-ray microbeam diffraction measurements were made at the Advanced Photon Source on beamline 34-ID in February and August 2007. Two samples with nominally identical structures were studied, one with white beam Laue diffraction in February and the other with monochromatic beam diffraction in August. The experimental setup is shown in Fig. 4. X rays could be switched between monochromatic mode and white beam mode. The x-ray beam was focused by Kirkpatrick–Baez mirror optics to ~1 μm for the monochromatic beam experiments and to ~0.4 μm for the white beam experiments. In the monochromatic mode, the x-ray energy was scanned over 60 eV with steps of 3 eV at each location across and along the Al line. The (333) diffraction peaks were recorded on the charge-coupled device (CCD) detector to obtain the (333) *d*-spacings for suitably oriented Al grains at each measurement location.[12] Using the lattice parameter[13,14] for pure Al, $a=0.4065$ nm for $T=190$ °C, the measured *d*-spacings were converted to perpendicular elastic strains. In the x-ray energy scan at each location, any (111) grain oriented within ±0.2° of the sample normal would contribute a (333) diffraction peak. The perpendicular elastic strain at each location is the average of the strains of all of the contributing (111) grains within the 1 μm x-ray beam.

In the white beam mode, the CCD detector collected Laue diffraction at each measurement location from grains with various orientations. Grain-scale determination of the local crystal orientations and local deviatoric elastic strains were obtained by indexing and fitting the Laue patterns.[15,16] The relationship between the normal deviatoric elastic strains $\varepsilon_{xx}^*, \varepsilon_{yy}^*, \varepsilon_{zz}^*$ and the full elastic strains $\varepsilon_{xx}, \varepsilon_{yy}, \varepsilon_{zz}$ is given by

$$\varepsilon_{xx}^* = \varepsilon_{xx} - \tfrac{1}{3}(\varepsilon_{xx} + \varepsilon_{yy} + \varepsilon_{zz}),$$

$$\varepsilon_{yy}^* = \varepsilon_{yy} - \tfrac{1}{3}(\varepsilon_{xx} + \varepsilon_{yy} + \varepsilon_{zz}),$$

$$\varepsilon_{zz}^* = \varepsilon_{zz} - \tfrac{1}{3}(\varepsilon_{xx} + \varepsilon_{yy} + \varepsilon_{zz}). \tag{2}$$

Note that $\varepsilon_{xx}^*+\varepsilon_{yy}^*+\varepsilon_{zz}^*=0$. By translating the sample, x rays scan the whole conductor line and the orientations and strains at each point of the scan are determined. The step size of the raster was 0.5 μm across and along the line in white beam measurements, and 0.5 μm across the line and 1.5 μm along the line for monochromatic beam measurements. Each cycle of measurements required about 3.6 h in the white beam mode and about 5.5 h in the monochromatic mode.

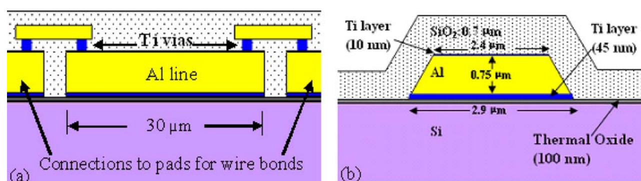

FIG. 2. (Color online) Schematic cross sections of the Al line. (a) Cross section along Al line shows Ti vias are at both ends of the Al line. (b) Cross section across the line shows the dimensions of the line.

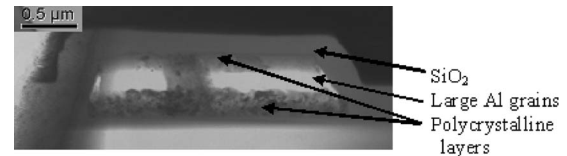

FIG. 3. TEM cross section shows small grain polycrystalline layers on the top and bottom of the large grain Al line.

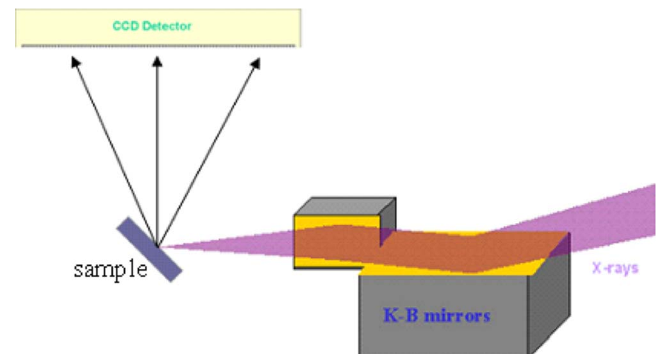

FIG. 4. (Color online) Schematic setup for x-ray microdiffraction experiments which can use a polychromatic or monochromatic x-ray beam.

Downloaded 16 Feb 2011 to 128.113.218.36. Redistribution subject to AIP license or copyright; see http://jap.aip.org/about/rights_and_permissions

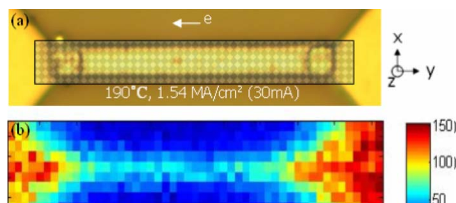

FIG. 5. (Color online) (a) Schematic x-ray mapping the Al conductor line. (b) Ti mapping with fluorescence intensity in arbitrary units.

III. RESISTANCE CHANGES DURING EM

The samples were heated to 190 °C and stressed with 30 mA current, corresponding to a current density of 1.54×10^6 A/cm^2. As indicated in Fig. 5(a), electrons flow from right to left. Ti fluorescence was used to locate the Al line, and Ti mapping is shown in Fig. 5(b). The coordinate system used to describe the direction of electron flow, the strain tensor, and the orientation of the specimen has X across the line width, Y along the line length opposite to the direction of electron flow, and Z normal to the line directed toward the substrate, as indicated in Fig. 5(a).

The resistances of the Al lines were monitored by measuring the voltage across the two ends of the conductor line, including voltage drops across the Ti vias. At 190 °C, the calculated resistance of the Al line is about 0.7 Ω, using the resistivity of 2.8×10^{-6} Ω cm and the thermal coefficient of resistivity 3.9×10^{-3} K^{-1} at 20 °C.[17] The measured values were 4.9 and 5.1 Ω for the two samples used for white and monochromatic beam measurements, respectively. Most of the observed resistance is believed to be contact resistance between the Al lines and the Ti vias and the Ti vias themselves. No resistance increases were seen during EM for either sample, indicating that no significant voids formed during EM.

For the sample used in the white beam measurements, the resistance as shown in Fig. 6(a) decreased gradually from 4.9 to 4.3 Ω during 37 h of EM. Superimposed on this gradual decrease were periodic, more rapid decreases in resistance, which occurred when the x-ray beam scanned over the area of the upstream Al/Ti via contacts. The period is the same as one cycle of x-ray scanning of the Al line, about 3.6 h. The periodic acceleration in the decrease of resistance could be due to the x-ray beam causing local heating and reducing the Al–Ti contact resistance by thermal expansion of these metals. The overall gradual decrease of resistance could be caused by improvement of the Al/Ti contact resistance by addition of Al atoms during EM. However, the resistance of the sample used for monochromatic measurements has neither gradual nor periodic decreases comparable to those of Fig. 6(a), as shown in Fig. 6(b). This may be due to four times larger x-ray beam size and for most of the measurement time using a monochromatic x-ray beam, which would cause less local heating. Another possible reason could be sample to sample variation during processing, since the contact resistance is expected to depend on the surface conditions of the Ti vias and Al line.

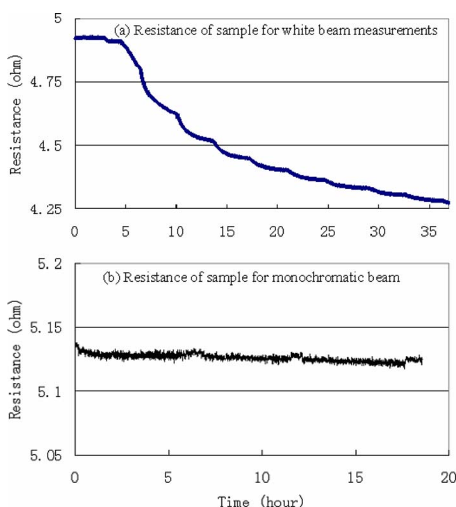

FIG. 6. (Color online) Resistance change during EM in two samples. (a) A periodic decrease in the sample for white beam measurements. (b) No significant resistance change in the sample for monochromatic beam measurements.

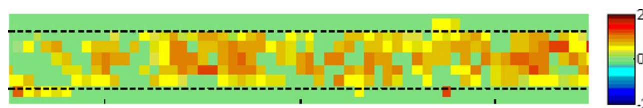

FIG. 7. (Color online) Map of strain ε^*_{zz} (unit of strain 10^{-3}) at 190 °C before EM. The dash line shows the boundaries of Al line.

IV. EVOLUTION OF STRAIN DURING EM

Figure 7 shows the map of deviatoric elastic strain ε^*_{zz} at 190 °C before EM. Strain values could not be obtained for some measurement locations. Missing strain data are due to the Laue patterns not being well fitted because of weak intensities and/or streaked Laue spots. Strain ε^*_{zz} varies with position on the line, ranging from -1×10^{-3} to 2×10^{-3}. In order to study the evolution of strains, averages across the line for ε^*_{yy} and ε^*_{zz} are plotted as a function of distance from the anode end of the line in Figs. 8(a)–8(j), which show the evolution of deviatoric elastic strains measured by white beam mode along the 30 μm long Al line during 25.2 h of EM. Since the raster from one end of the line to the other end takes about 3.6 h, and the measurement sequence is from left to right (anode end to cathode end), the strain values on the right end were measured 3.6 h later than those on the left end. Before EM at 190 °C and during the first 3.6 h of EM, there is no significant strain gradient along the line for either ε^*_{yy} or ε^*_{zz}. The deviatoric elastic strain gradient began to form during 7.2–10.8 h of EM, and it saturated after about 14 h of EM.

Figures 9(a) and 9(b) show the out-of-plane and in-plane orientation maps of the Al line used in the white beam strain measurements at room temperature before EM. From Fig. 9(a), the Al line has a strong (111) preferred orientation, which makes the monochromatic (333) diffraction measurements possible. The in-plane orientation map in Fig. 9(b) shows that the line has a near-bamboo grain structure, with most grains spanning the width of the line.

Figure 10 shows the map of elastic strain ε_{zz} at 190 °C before EM measured by monochromatic mode. Monochromatic strain measurements could not be obtained near the

Downloaded 16 Feb 2011 to 128.113.218.36. Redistribution subject to AIP license or copyright; see http://jap.aip.org/about/rights_and_permissions

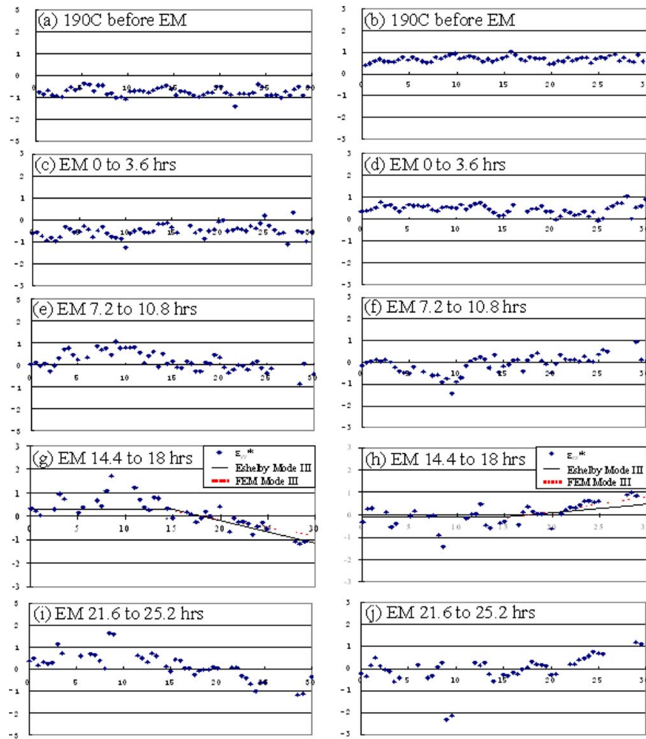

FIG. 8. (Color online) [(a)–(j)] Deviatoric strain ε_{yy}^* and ε_{zz}^* along the 30 μm long Al conductor line, with electron flow from right to left during EM. The horizontal axis is distance along the line, and vertical axis is the deviatoric strain. The plots on the left show ε_{yy}^* and on the right show ε_{zz}^*. The unit of strain is 10^{-3}. Trend lines in (g) and (h) are from the Eshelby and FE model mode III calculations.

ends of the conductor line, where data points are missing in Fig. 10. This may be due to higher Ti concentration on both ends of the line, as suggested by Fig. 5(b). Figures 11(a)–11(d) show plots of ε_{zz} averaged across the linewidth as a function of distance to the anode end before and during EM. There is considerably less scatter in the full perpendicular elastic strain results than in the deviatoric elastic strain results. Since the x-ray beam size was about 1 μm in the monochromatic mode measurements and about 0.4 μm in the white beam mode measurements, the full perpendicular elastic strain measured in the monochromatic mode averages over several near (111) grains contained within a larger irradiated area at each measurement location, whereas each of the deviatoric strain measurements is for a single grain, or part of a grain, within a smaller irradiated area, in some cases including non-(111) grains.

There is a "dip" in ε_{zz} near the middle of the line at 190 °C before EM, as shown in Fig. 11(a), which may be also due to the higher Ti concentration near the ends of the line increasing the lattice parameter and increasing the apparent values of ε_{zz}. This dip is not seen in the white beam mode measurements at 190 °C before EM. One possible reason is that the microstructure is different in the two samples. Another possible reason is that the difference in Ti concentration affects the hydrostatic strains but not deviatoric strains. A strain gradient began to form in ε_{zz} along the upstream part of the line during the first 5.5 h and saturated after 12 h, similar to the results seen for ε_{yy}^* and ε_{zz}^* in the other sample.

Wang *et al.*[6] also found a linear EM-induced perpendicular strain gradient, but with the opposite sign compared with our result and extending along the full length of the conduc-

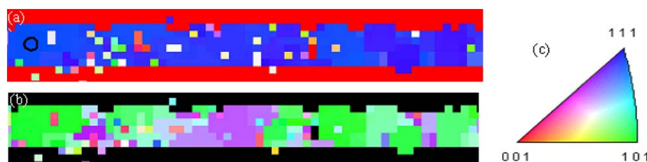

FIG. 9. (Color online) (a) Out-of-plane orientation map. (b) In-plane orientation map. (c) Orientation legend. The black circle in (a) shows the measurement location for the Laue spot images in Fig. 17.

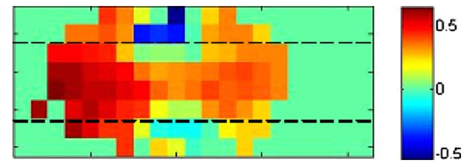

FIG. 10. (Color online) Map of strain ε_{zz} (unit of strain is 10^{-3}) at 190 °C before EM. The two dash lines show the boundaries of the Al line.

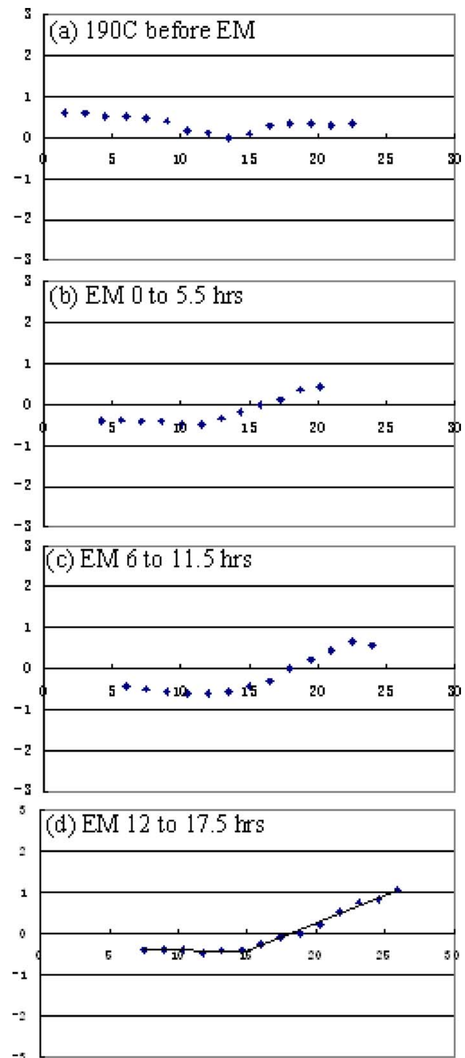

FIG. 11. (Color online) [(a)–(d)] Full perpendicular elastic strain ε_{zz} along the 30 μm long Al line, with electron flow from right to left during EM. The horizontal axis is the distance along the line, and vertical axis is the full perpendicular strain. The unit of strain is 10^{-3}.

Downloaded 16 Feb 2011 to 128.113.218.36. Redistribution subject to AIP license or copyright; see http://jap.aip.org/about/rights_and_permissions

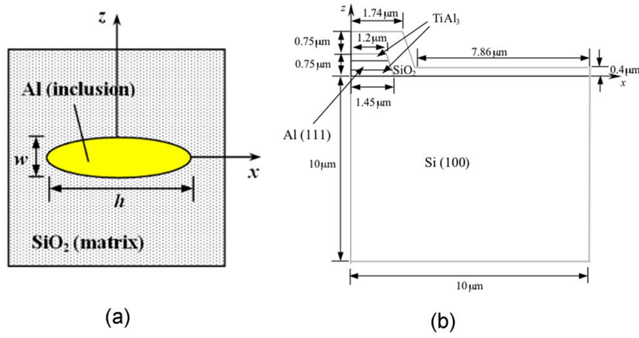

FIG. 12. (Color online) (a) Eshelby model. (b) FE model (not to scale).

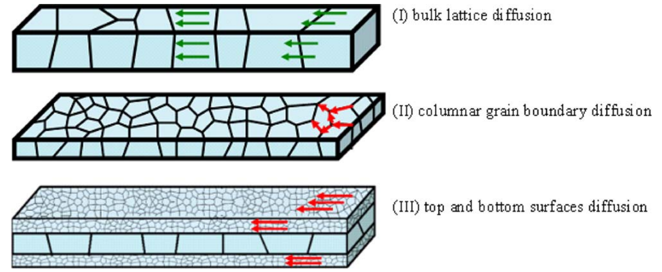

FIG. 13. (Color online) Three different EM modes.

tor line. In their case, the Al line was 10 μm wide with polycrystalline columnar grain structure, for which EM was expected to be mainly along the grain boundaries, causing the ε_{xx} and ε_{yy} in-plane compressive strains at the downstream end. The measured positive perpendicular tensile strain ε_{zz} at the downstream end was attributed to the Poisson effect in their case.

V. MODELS RELATING EM-INDUCED STRAINS TO ELASTIC STRAINS

In order to investigate the EM diffusion path in these Al lines, Eshelby and FE models were used to relate the inelastic (stress-free) strain resulting from EM-induced diffusion to the elastic strain and then compared to the experimental measurements. In the Eshelby model, the Al line is treated as an elliptic cylinder surrounded by an infinite SiO_2 matrix, while in the FE calculations, the true layered structure and dimensions of the Al line are used in the strain calculation, as depicted in Figs. 12(a) and 12(b), where only half the domain needs to be considered in the FE model because of symmetry.

Both the Eshelby and the FE models treat the aluminum line and surrounding materials as linear elastic and in stress equilibrium. Let Ω be the entire problem domain, and then the following equations of elasticity and equilibrium must be satisfied on Ω:

$$\sigma_{ij} = C_{ijkl}\varepsilon_{kl}, \tag{3}$$

$$\varepsilon_{ij} = \varepsilon_{ij}^{T} - \varepsilon_{ij}^{\mathrm{EM}}, \tag{4}$$

$$\varepsilon_{ij}^{T} = \tfrac{1}{2}(u_{i,j} + u_{j,i}), \tag{5}$$

$$\sigma_{ij,j} = 0, \tag{6}$$

where σ_{ij} is the Cauchy stress, ε_{ij} is the elastic strain, C_{ijkl} is the elasticity tensor, ε_{ij}^{T} is the total strain, $\varepsilon_{ij}^{\mathrm{EM}}$ is the EM-induced inelastic strain (only nonzero in the aluminum line), u_i is the displacement, and comma denotes derivative $(,j \equiv \partial/\partial x_j)$.

Three different EM-induced diffusion paths are considered, as shown schematically in Fig. 13, similar to the analysis considered in Hau-Riege and Thompson.[9] In mode I, diffusion is throughout the line, so atoms are deposited (or depleted) equally in all three directions. In mode II, diffusion is through the grain boundaries in a columnar grain structure, so atoms are deposited in the plane of the line. In mode III, diffusion is primarily along the top and bottom interfaces, so atoms are deposited in the thickness direction. The inelastic strains resulting from each of these modes are as follows.

For mode I,

$$\varepsilon_{xx}^{\mathrm{EM}} = \varepsilon_{yy}^{\mathrm{EM}} = \varepsilon_{zz}^{\mathrm{EM}} = \frac{\Delta}{3}; \tag{7a}$$

for mode II,

$$\varepsilon_{xx}^{\mathrm{EM}} = \varepsilon_{yy}^{\mathrm{EM}} = \frac{\Delta}{2}, \quad \varepsilon_{zz}^{\mathrm{EM}} = 0; \tag{7b}$$

for mode III,

$$\varepsilon_{xx}^{\mathrm{EM}} = \varepsilon_{yy}^{\mathrm{EM}} = 0, \quad \varepsilon_{zz}^{\mathrm{EM}} = \Delta, \tag{7c}$$

where Δ is the local change in volume per unit volume. In the downstream end, Δ is positive as atoms are being deposited, and in the upstream end, where atoms are being depleted, Δ is negative.

A. Eshelby model

The Eshelby model used here is based on the model derived by Korhonen *et al.*[18] The relationship between the EM strain and the stress is[18]

$$\varepsilon_{ij}^{\mathrm{EM}} = (T_{ijkl} + S_{ijkl}^{M} - S_{ijkl}^{L})\sigma_{kl}, \tag{8}$$

where S_{ijkl}^{M} and S_{ijkl}^{L} are the compliance tensors ($S_{ijkl}=C_{ijkl}^{-1}$) of the SiO_2 matrix and Al line, respectively, $T_{ijkl}=(K-I)_{ijmn}^{-1}S_{mnkl}^{M}$, K_{ijkl} is the Eshelby tensor, and I_{ijkl} is the fourth order identity tensor. Using Eqs. (3) and (8), the EM strain can then be related to the elastic strain

$$\varepsilon_{ij}^{\mathrm{EM}} = (T_{ijkl} + S_{ijkl}^{M} - S_{ijkl}^{L})C_{klmn}^{L}\varepsilon_{mn} = [(T_{ijkl} + S_{ijkl}^{M})C_{klmn}^{L} - I_{ijmn}]\varepsilon_{mn}. \tag{9}$$

The SiO_2 matrix is treated as isotropic with an elastic modulus of $E=73.7$ GPa and Poisson's ratio of $\nu=0.17$.[19] The Al properties at 190 °C for a single crystal are from Ref. 20 and the line is treated as having a strong (111) texture with the in-plane orientation being random resulting in elastic stiffnesses, with respect to the laboratory coordinates, $C_{11}=C_{22}=107.1$ GPa, $C_{33}=108.7$ GPa, $C_{12}=59.2$ GPa, $C_{13}=C_{23}=57.5$ GPa, $C_{44}=C_{55}=22.3$ GPa, and $C_{66}=23.9$ GPa. The thickness and width of the Al line, neglecting the Ti rich layers above and below the line, are $h=0.35$ μm and $w=2.6$ μm. The results from the Eshelby model are summarized in Table I, where the elastic strains are normalized by

Downloaded 16 Feb 2011 to 128.113.218.36. Redistribution subject to AIP license or copyright; see http://jap.aip.org/about/rights_and_permissions

TABLE I. Eshelby model results compared with FEM results for three different EM modes.

		Normalized full elastic strains			Normalized deviatoric elastic strains		
		ε_{xx}/Δ	ε_{yy}/Δ	ε_{zz}/Δ	$\varepsilon^*_{xx}/\Delta$	$\varepsilon^*_{yy}/\Delta$	$\varepsilon^*_{zz}/\Delta$
Mode I	Eshelby (r=0.35/2.6)	−0.2690	−0.3333	0.2736	−0.1595	−0.2238	0.3832
	FEM	−0.2561	−0.3333	0.2727	−0.1505	−0.2278	0.3783
Mode II	Eshelby (r=0.35/2.6)	−0.3860	−0.5000	0.4258	−0.2326	−0.3466	0.5792
	FEM	−0.3740	−0.5000	0.4275	−0.2251	−0.3512	0.5763
Mode III	Eshelby (r=0.35/2.6)	−0.0351	0.0000	−0.0306	−0.0132	0.0219	−0.0087
	FEM	−0.0203	0.0000	−0.0367	−0.0013	0.0190	−0.0177

the dilatation. It shows that modes I and II generate strains with the opposite signs from our experimental results. Only mode III gives strains with the same sign as our experimental result.

B. Finite element model

A standard, two-dimensional, FE formulation is used to solve the governing equations (3)–(7). The variational form, neglecting body forces and assuming no traction boundary conditions, is given by

$$\int_{\Omega} C_{ijkl}\varepsilon^{T}_{kl}\bar{\varepsilon}_{ij}dV = \int_{\Omega_L} C_{ijkl}\varepsilon^{\mathrm{EM}}_{kl}\bar{\varepsilon}_{ij}dV, \qquad (10)$$

where $\bar{\varepsilon}_{ij}$ is an admissible variation in the total strain and Ω_L is the domain of the Al line, where the EM-induced strains are applied. The total strain ε^{T}_{ij} is expressed in terms of the displacement field in Eq. (5), which is interpolated with bilinear, quadrilateral elements and similarly for $\bar{\varepsilon}_{ij}$. The horizontal displacements on the left boundary and the vertical displacements on the bottom boundary are fixed. Equation (10) is solved for the displacement field, which is used to construct ε^{T}_{ij}. The elastic strains in the Al are then computed using Eq. (4). The same elastic properties for the SiO_2 and Al are used here as were used in the Eshelby model. For the Si substrate, which has a (100) orientation, the elastic properties at 190 °C are C_{11}=158 GPa, C_{12}=58 GPa, and C_{44} =79 GPa.[21] The $TiAl_3$ layers above and below the Al line are both assumed to be 0.2 μm in thickness, and the $TiAl_3$ is treated as isotropic with elastic modulus E=170 GPa and Poisson's ratio ν=0.25.[22]

The results are presented in Table I and Fig. 14. Table I provides a comparison to the Eshelby results, where the elastic strains are averaged in the cross section of the Al line. The results are similar. Figure 14(a) shows the predicted distribution of the ε_{zz} component of the elastic strain in the Al for the mode III case with $\Delta=3\times10^{-3}$ on the downstream end, where the material is assumed to be deposited in the top and bottom interfaces, and Fig. 14(b) shows the distribution across the width, averaged through the thickness. With the EM strain prescribed uniformly in the cross section, we see that a strong elastic strain gradient across the width of the line is predicted, with tensile strains in the center and compressive strains at the edges. This result is not physically reasonable since the high elastic strain gradients would lead to high stress gradients, which, in turn, would drive diffusion to reduce the stress gradient. Furthermore, such elastic strain gradients across the width are not observed in our measurements.

To obtain a more physically reasonable relationship between the EM-induced strain and the elastic strain, we solve an inverse problem where the elastic strain component ε_{zz} is prescribed and assumed to be uniform, and we reconstruct an EM-induced strain distribution in the cross section required to generate the uniform elastic strain. Focusing on mode III case, which is the most relevant case here, let the EM and total strains be expressed as

$$\varepsilon^{\mathrm{EM}}_{ij} = \Delta Q_{ij}, \qquad (11)$$

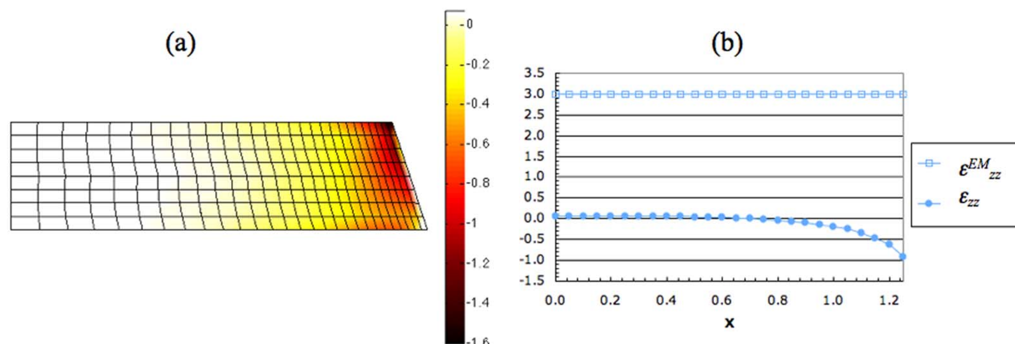

FIG. 14. (Color online) (a) Elastic strain ε_{zz} distribution predicted by FE simulation for uniform EM-induced strain $\varepsilon^{\mathrm{EM}}_{zz}=\Delta=3.0\times10^{-3}$. (b) Distributions of ε_{zz} and $\varepsilon^{\mathrm{EM}}_{zz}$ across the width of the line, averaged through the thickness.

Downloaded 16 Feb 2011 to 128.113.218.36. Redistribution subject to AIP license or copyright; see http://jap.aip.org/about/rights_and_permissions

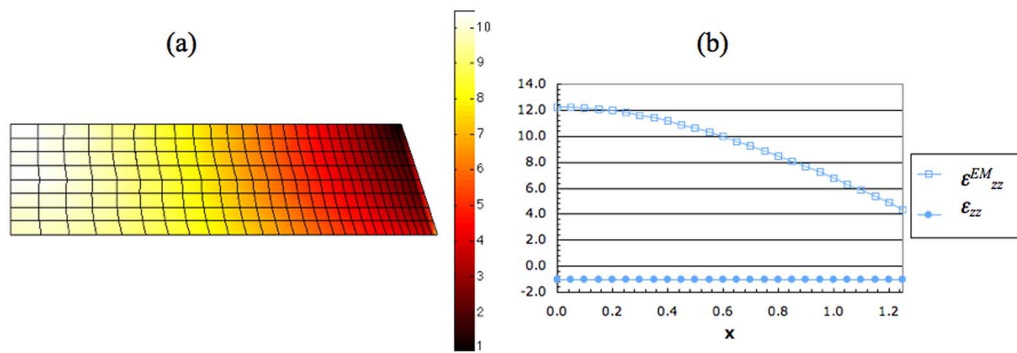

FIG. 15. (Color online) (a) EM-induced strain $\varepsilon_{zz}^{\mathrm{EM}}$ distribution predicted by FE simulation for uniform elastic strain $\varepsilon_{zz}=-10^{-3}$. (b) Distributions of ε_{zz} and $\varepsilon_{zz}^{\mathrm{EM}}$ across the width of the line, averaged through the thickness.

$$\varepsilon_{ij}^{T}=\bar{\varepsilon}_{ij}^{T}+\varepsilon_{zz}^{T}Q_{ij}, \qquad (12)$$

where Q_{ij} is a matrix that is zeros everywhere except $Q_{zz}=1$, and Eq. (12) represents a partitioning of the total strain. Note that the elastic strain component, which is to be prescribed, is $\varepsilon_{zz}=\varepsilon_{zz}^{T}-\Delta$ for mode III case. Substituting Eqs. (11) and (12) into Eq. (10) results in the following variational formulation:

$$\int_{\Omega L} C_{ijkl}\bar{\varepsilon}_{kl}^{T}\bar{\varepsilon}_{ij}dV=\int_{\Omega L}\varepsilon_{zz}C_{ijkl}Q_{kl}\bar{\varepsilon}_{ij}dV \qquad (13)$$

in the Al line. This equation combined with a standard elastic formulation in the remaining materials, after substituting in the FE interpolations functions, results in a system of equations for the displacement field. However, Eq. (13) is ill posed and does not have a unique solution.

In order to obtain a unique solution, we express Eq. (13) as an energy minimization problem with a first order regularization term to impose smoothness on the displacement field, which reduces fluctuations in the strain fields. The following modified variational formulation results

$$\int_{\Omega L} C_{ijkl}\bar{\varepsilon}_{kl}^{T}\bar{\varepsilon}_{ij}dV+\alpha\int_{\Omega L} u_{i,j}\bar{u}_{i,j}dV =\int_{\Omega L}\varepsilon_{zz}C_{ijkl}Q_{kl}\bar{\varepsilon}_{ij}dV, \qquad (14)$$

where α is a regularization parameter. From the displacement field, the total strain can be computed, and then the EM strain is recovered from $\Delta=\varepsilon_{zz}^{T}-\varepsilon_{zz}$. For a uniform prescribed elastic strain of $\varepsilon_{zz}=-10^{-3}$, the resulting EM-induced strain distribution is shown in Fig. 15(a), and the distribution across the width is shown in Fig. 15(b), where the strains are averaged through the thickness. The result shows that a greater amount of material is deposited toward the center of the line than at the edges. Note that although the solution shows a fairly uniform EM-induced strain through the thickness, the actual material is likely deposited in the top and bottom interfaces. However, the resulting elastic strain field is not affected much by where in the thickness the atoms are deposited (e.g., through the thickness versus in the interfaces). In fact, this lack of uniqueness is why the inverse problem is ill posed.

Referring again to Table I, which gives the relationships between the EM-induced local volume change [see Eq. (7)] and the deviatoric and full elastic strains for the Eshelby and FE models, we compare these results to our experimental measurements. Based on the full perpendicular strain, one can predict the deviatoric strains. Using the ε_{zz} trend line in Fig. 11(d), the lines in Figs. 8(g) and 8(h) are resulting predictions of ε_{yy}^{*} and ε_{zz}^{*} for mode III EM. Both the Eshelby model and FE calculations for mode III EM agree well with the ε_{yy}^{*} experimental results, but the FE calculations give significantly better agreement than the Eshelby model for ε_{zz}^{*}.

VI. STRAIN RELAXATION

A linear strain gradient formed in the upstream part of the Al line, but no gradient formed in the downstream part of the line, as shown in Figs. 8(g)–8(j) and 11(d). This could be the result of strain relaxation in the downstream part of the conductor line, due to the plastic deformation or material leakage, resulting from delamination of the passivation layer. Figures 16(a)–16(c) show schematically how a crack could start to form and cause delamination of the passivation layer and strain relaxation in the downstream end of the Al line.

Before EM, the thickness of the line is the same everywhere along the line, as in Fig. 16(a). With EM, additional Al atoms move into the downstream end of the line, along the top and bottom surfaces, pushing the passivation layer up and causing cracks to form in the bottom surface, as shown in Fig. 16(b). After the cracks form, further addition of Al atoms on the top and bottom surfaces causes the crack to propagate across and along the Al line, leading to further delamination, as shown in Fig. 16(c). When the passivation layer delaminates, it provides less confinement of the Al line

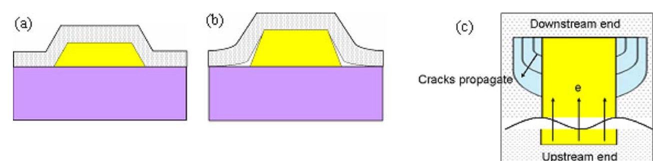

FIG. 16. (Color online) (a) Cross section of Al line in the downstream end, before EM. (b) During EM, Al line becomes thicker and pushes the passivation layer up to form cracks. (c) As EM continues, the cracks propagate across, and along the line.

Downloaded 16 Feb 2011 to 128.113.218.36. Redistribution subject to AIP license or copyright; see http://jap.aip.org/about/rights_and_permissions

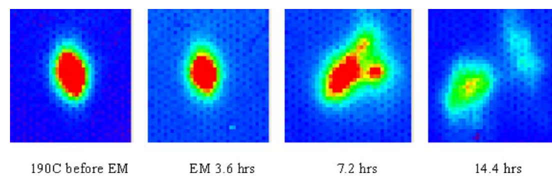

FIG. 17. (Color online) Laue diffraction spot from the location in the downstream end of the line, shown in Fig. 9(a), at different times before and during EM.

and the strains in the downstream part of the lines relax, which may be the reason that no strain gradient is seen in the downstream part of the lines.

From Table I and the observed ε_{zz}, as shown in Fig. 11(d), the magnitude of ε_{zz}^{T*} is estimated to be about 5% at the downstream end of the line using the FE calculation result with EM mode III, which corresponds to an increase of about 450 nm$\times$5%=23 nm in the conductor line thickness at the downstream end. It would be difficult to detect such a small change in thickness along the line using optical imaging, SEM, or atomic force microscope, because the roughness of the sample is also is of this order.

Plastic deformation during EM, another path for strain relaxation, can be detected from the evolution of Laue diffraction patterns. Figure 17 shows the evolution of one spot in the Laue diffraction pattern from the measurement location shown by the black circle in Fig. 9(a). Before EM and during the first 3.6 h, spots in the Laue patterns are sharp and are not split. After 7.2 h, some of the single Laue spots start to split into two or more spots. After 14.4 h, some single spots are completely divided into two spots and the diffraction intensities drop. The splitting of the Laue spots indicates that plastic deformation occurs during EM, resulting in the formation of new grains with different orientations. Figures 18(a)–18(e) show the evolution of in-plane orientation maps of the line. The grain orientations, especially at locations near the ends, change during EM, sometimes by large amounts, indicating that recrystallization, as well as plastic deformation, has occurred. Similar observations have been reported by Valek *et al.*[23,24]

By plastic deformation and by recrystallization, the elastic strain energy is lowered. The more scattered data of the deviatoric strains in the downstream part of the conductor line may result from local strain relaxation by plastic deformation and by recrystallization. A more comprehensive model, taking into account delaminations and plastic strains, may be required to better understand the strain evolution of the line during EM.

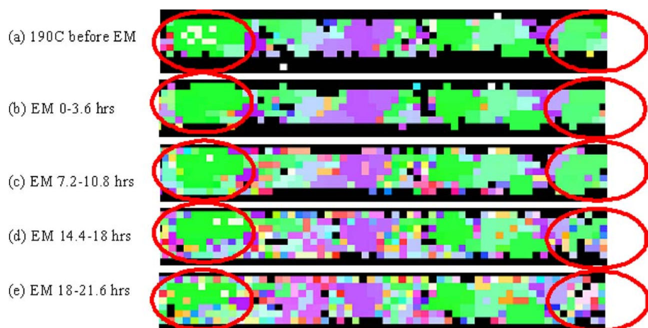

FIG. 18. (Color online) In-plane orientation evolution during EM. Legend is shown in Fig. 9(c). The large grains on both ends break up into smaller grains during EM.

VII. EFFECTIVE VALENCE Z^* FROM STRAIN GRADIENT MEASUREMENTS

Since both the full perpendicular strains and deviatoric strains have been measured, the hydrostatic strain and hydrostatic strain gradient can be calculated using Eq. (2). Assuming that the EM has reached a steady state in our experiments with $j<j_c$, and using $b=1$ for the hydrostatic case, from Eq. (1) it follows that

$$|Z^*| = \frac{\partial \sigma_{\mathrm{EM}}}{\partial y}\frac{\Omega}{ej\rho}. \tag{15}$$

As described in the Appendix, $|Z^*|$ is calculated to be 1.8 ± 0.4 (60% confidence level) from our measurements, in good agreement with values of $|Z^*|$ for Al conductor from other types of measurements and experimental conditions. Blech *et al.*[5] reported $|Z^*|\sim1.2$ from their measurements on 50 μm wide unpassivated Al lines. Chiras *et al.*[25] reported $|Z^*|=1.3\pm0.2$ from measurements of 5 μm wide passivated Al lines. Wang *et al.*[6] reported $|Z^*|=1.6$ from measurements on 10 μm wide SiO_2 passivated Al lines. The value of Z^* indicates the strength of interaction between electrons and atoms during EM. The effect of EM mode, temperature, and microstructure on Z^* has not been systematically studied, either experimentally or theoretically, and are not well understood.

VIII. CONCLUSIONS

Deviatoric and full perpendicular strain measurements were carried out during EM in Al conductor lines with near-bamboo structures. A strong strain gradient developed in the upstream part of the Al lines and no strain gradient developed in the downstream part of the lines. The experimental results and numerical calculations using the Eshelby model and FEM method suggest that that the EM is mainly along the top and bottom interfaces, with less EM flux near the edges of the line than near the center. Evidence of plastic deformation is seen in the evolution of the Laue diffraction patterns. A value of $|Z^*|=1.8\pm0.4$ is obtained from the measured strain gradient.

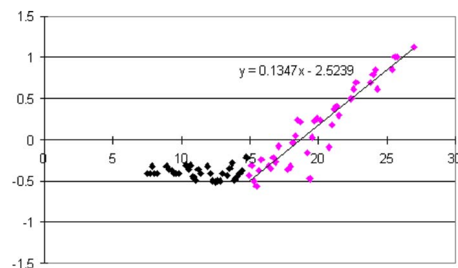

FIG. 19. (Color online) Fitting of $y(x)=\varepsilon_{zz}(x)$ during EM 12 to 17.5 h of monobeam measurements in the upstream end of the conductor line.

Downloaded 16 Feb 2011 to 128.113.218.36. Redistribution subject to AIP license or copyright; see http://jap.aip.org/about/rights_and_permissions

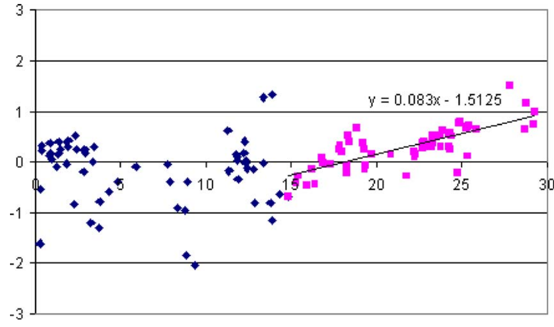

FIG. 20. (Color online) Fitting of $y(x)=\varepsilon^*_{zz}(x)$ during EM of 14.4–18 h of white beam measurements in the upstream end of the conductor line.

ACKNOWLEDGMENTS

This research was supported by NSF, Grant No. DMR-0312189. Samples were provided by Dr. T. Marieb, Intel Corp. The x-ray diffraction experiments were carried out on beamline 34ID at APS, Argonne National Laboratory, which is supported by the U.S. DOE.

APPENDIX: CALCULATION OF Z^* FROM STRAIN GRADIENT MEASUREMENTS

From Eq. (1), the relationship between $|Z^*|$ and the steady-state strain gradient for current density j smaller than the critical current density j_c is given by

$$|Z^*| = b\frac{\partial \sigma_{\mathrm{EM}}}{\partial y}\frac{\Omega}{ej\rho}, \quad (A1)$$

where b is a stress state-dependent coefficient, with $b=1$ if σ_{EM} is the hydrostatic stress, $\partial\sigma_{\mathrm{EM}}/\partial y$ is EM-induced stress gradient along the length of the conductor line, Ω is the atomic volume, e is the electron charge, j is the current density, and ρ is the electrical resistivity of Al.

The hydrostatic component of the stress is given by

$$\sigma_{\mathrm{EM}} = B\frac{\Delta V}{V} = 3B(\varepsilon_{zz} - \varepsilon^*_{zz}) \quad (A2)$$

wherer B is the bulk modulus of Al, and the gradient of this stress is

$$\frac{\partial \sigma_{\mathrm{EM}}}{\partial y} = 3B\left(\frac{\partial \varepsilon_{zz}}{\partial y} - \frac{\partial \varepsilon^*_{zz}}{\partial y}\right), \quad (A3)$$

where $\partial\varepsilon_{zz}/\partial y$ and $\partial\varepsilon^*_{zz}/\partial y$ are determined by fitting the strain gradient in the monochromatic mode and white beam mode measurements, as shown in Figs. 19 and 20. The resulting expression for the effective valence is then

$$|Z^*| = 3bB\left(\frac{\partial \varepsilon_{zz}}{\partial y} - \frac{\partial \varepsilon^*_{zz}}{\partial y}\right)\frac{\Omega}{ej\rho}. \quad (A4)$$

Uncertainty in $|Z^*|$ comes mainly from the errors in fitting the strain gradients. The values of terms in Eq. (A4) are given as[17]

TABLE II. Uncertainties for different confidence levels r.

r	0.95	0.9	0.8	0.6
K_{white}	0.0189	0.0159	0.0123	0.0080
K_{mono}	0.0157	0.0131	0.0101	0.0066
K_{total}	0.0246	0.0206	0.0159	0.0104

$$b = 1,$$

$$B = 76 \text{ GPa},$$

$$\Omega = 1.7 \times 10^{-23} \text{ cm}^3,$$

$$e = 1.6 \times 10^{-19} \ C = 1.6 \times 10^{-19} \text{ A s},$$

$$j = 1.54 \times 10^{6} \text{ A/cm}^2,$$

$$\rho = 4.54 \times 10^{-6} \ \Omega \text{ cm},$$

$$\frac{\partial \varepsilon_{zz}}{\partial x} = 0.1347 \times 10^{-3} \pm K_{\mathrm{mono}} \ \mu\text{m}^{-1},$$

$$\frac{\partial \varepsilon^*_{zz}}{\partial y} = 0.083 \times 10^{-3} \pm K_{\mathrm{mono}} \ \mu\text{m}^{-1},$$

where K_{mono} and K_{white} are the fitting errors for the slopes of ε_{zz} and ε^*_{zz}, respectively. For a least squares fitting $Y=A+BX$ of number of n independent data points, there is a fitting uncertainty K, $Y=A+(B\pm K)X$, where K depends on the confidence level.

Values of K_{mono} and K_{white} were determined as follows.[26]

(1) The value of c is obtained from the t-distribution table with $n-2$ degrees of freedom (Table A9, Appendix 5),[26] $F(c)=0.5(1+r)$, where r is the confidence level.

(2) The standard deviations are calculated for best straight line fits to $y(x)=\varepsilon_{zz}(x)$ and $y(x)=\varepsilon^*_{zz}(x)$, where x represents distance along the length of the conductor line, and the fits are made over the ranges shown in Figs. 19:

$$S_x^2 = \frac{1}{n-1}\sum (x_i - \bar{x})^2, \quad S_y^2 = \frac{1}{n-1}\sum (y_i - \bar{y})^2.$$

(3) The uncertainties are calculated for the chosen confidence levels

$$K = c\sqrt{\frac{(S_y^2 - B^2 S_x^2)}{(n-2)S_x^2}}.$$

Table II shows the fitting uncertainties in white beam measurements and monobeam measurements, for four different confidence levels. The total uncertainty in Z^* depends on $K_{\mathrm{total}}=\sqrt{K_{\mathrm{white}}^2+K_{\mathrm{mono}}^2}$.The terms in Eq. (A4) for $|Z^*|$ were evaluated using the values given above:

TABLE III. Uncertainties ΔZ^* in $|Z^*|$.

r	0.95	0.90	0.80	0.60
ΔZ^*	0.85	0.71	0.55	0.37

Downloaded 16 Feb 2011 to 128.113.218.36. Redistribution subject to AIP license or copyright; see http://jap.aip.org/about/rights_and_permissions

$$\frac{\partial \varepsilon_{zz}}{\partial y} - \frac{\partial \varepsilon_{zz}^*}{\partial y} = [(0.1347 - 0.083) \pm K_{\text{total}}] \times 10^{-3}\ \ \mu\text{m}^{-1} = (0.0517 \pm K_{\text{total}}) \times 10^{-3}\ \ \mu\text{m}^{-1},$$

$$\frac{\Omega}{ej\rho} = \frac{1.7 \times 10^{-23}\ \ \text{cm}^3}{1.6 \times 10^{-19}\ \ \text{A s} \times 1.54 \times 10^{-6}\ \ \text{A/cm}^2 \times 4.54 \times 10^{-6}\ \ \Omega\ \text{cm}} = 1.52 \times 10^{-7}\ \ \text{cm}^3/\text{N},$$

$$Z^* = 3bB\left(\frac{\partial \varepsilon_{zz}}{\partial y} - \frac{\partial \varepsilon_{zz}^*}{\partial y}\right)\frac{\Omega}{ej\rho} = 1.8 \pm 34.6\ \ K_{\text{total}}.$$

Table III shows the uncertainties of $|Z^*|$ for difference confidence levels. For the 60% confidence level, $|Z^*| = 1.8 \pm 0.4$.

[1] H. B. Huntington and A. R. Grone, Phys. Chem. Solids **20**, 76 (1961).
[2] R. F. Liu, C.-K. Hu, L. Gignac, J. M. E. Harper, J. Lloyd, X.-H. Liu, and A. K. Stamper, J. Appl. Phys. **95**, 3737 (2004).
[3] K. N. Tu, J. Appl. Phys. **94**, 5451 (2003).
[4] R. Rosenberg, D. Edelstein, C.-K. Hu, and K. P. Rodbell, Annu. Rev. Mater. Sci. **30**, 229 (2000).
[5] I. A. Blech and K. L. Tai, Appl. Phys. Lett. **30**, 387 (1977).
[6] P.-C. Wang, G. S. Cargill III, I. C. Noyan, and C.-K. Hu, Appl. Phys. Lett. **72**, 1296 (1998).
[7] M. A. Korhonen, P. Børgesen, K. N. Tu, and C.-Y. Li, J. Appl. Phys. **73**, 3790 (1993).
[8] J. D. Eshelby, Proc. R. Soc. London, Ser. A **241**, 376 (1957).
[9] S. P. Hau-Riege and C. V. Thompson, J. Mater. Res. **15**, 1797 (1999).
[10] H. Zhang, G. S. Cargill III, Y. Ge, A. M. Maniatty and W. Liu, Mater. Res. Soc. Symp. Proc. **1027**, D01 (2008).
[11] H. Zhang, G. S. Cargill III, Y. Ge, A. M. Maniatty, and W. Liu, *Conference Proceeding AMC XXIII*, Materials Research Society, p. 727 (2008).
[12] L. E. Levine, B. C. Larson, W. Yang, M. E. Kassner, J. Z. Tischler, M. A. Delos-Reyes, R. J. Fields, and W. Liu, Nature Mater. **5**, 619 (2006).
[13] R. W. G. Wyckoff, *Crystal Structures*, 2nd ed. (Interscience, New York, 1963).
[14] O. Kraft and W. D. Nix, J. Appl. Phys. **83**, 3035 (1998).
[15] G. E. Ice and B. C. Larson, Adv. Eng. Mater. **2**, 643 (2000).
[16] J.-S. Chung and G. E. Ice, J. Appl. Phys. **86**, 5249 (1999).
[17] R. C. Weast, *CRC Handbook of Chemistry and Physics*, 64th ed. (CRC, Boca Raton, FL, 1983), p. E-78.
[18] M. A. Korhonen, R. D. Black, and C.-Y. Li, J. Appl. Phys. **69**, 1748 (1991).
[19] E. H. Bogardus, J. Appl. Phys. **36**, 2504 (1965).
[20] J. L. Tallon and J. Wolfenden, J. Phys. Chem. Solids **40**, 831 (1979).
[21] S. Adachi, *Handbook on Physical Properties of Semiconductors* (Kluwer Academic, Dordrecht, 2004).
[22] C. L. Fu, J. Mater. Res. **5**, 971 (1990).
[23] B. C. Valek, J. C. Bravman, N. Tamura, A. A. MacDowell, R. S. Celestre, H. A. Padmore, R. Spolenak, W. L. Brown, B. W. Batterman, and J. R. Patel, Appl. Phys. Lett. **81**, 4168 (2002).
[24] B. C. Valek, N. Tamura, R. Spolenak, W. A. Caldwell, A. A. MacDowell, R. S. Celestre, H. A. Padmore, J. C. Bravman, B. W. Batterman, W. D. Nix, and J. R. Patel, J. Appl. Phys. **94**, 3757 (2003).
[25] S. Chiras and D. R. Clarke, J. Appl. Phys. **88**, 6302 (2000).
[26] E. Kreyszig, *Advanced Engineering Mathematics*, 8th ed. (Wiley, New York, 1999).

Downloaded 16 Feb 2011 to 128.113.218.36. Redistribution subject to AIP license or copyright; see http://jap.aip.org/about/rights_and_permissions